# Self-modified breaking hydrogen bonds to highly crystalline graphitic carbon nitrides nanosheets for drastically enhanced hydrogen production

Waheed Iqbal[1], Bocheng Qiu[1], Qiaohong Zhu[1], Mingyang Xing, Jinlong Zhang*

*Key Laboratory for Advanced Materials and Institute of Fine Chemicals, School of Chemistry and Chemical Engineering, East China University of Science and Technology, 130-Meilong Road, Shanghai 200237, PR China*

ABSTRACT

Highly crystalline graphitic carbon nitride (g-$C_3N_4$) possesses the high separation efficiency of photogenerated electron-hole pairs owing to the significantly decreased intralayer hydrogen bonds, which leads to drastic improvement of photocatalytic activity. However, the preparation of such g-$C_3N_4$ material remains a challenge by a simple and economic thermal-treatment in a furnace. Herein, we report a novel and effective strategy for high-yield synthesis of extremely active crystalline carbon nitride nanosheets (CCNNSs) by two-step calcination without the assistance of any additive or salt intercalation. As expected, the as-prepared CCNNSs exhibit a remarkably high hydrogen evolution rate of 9577.6 $\mu$mol h$^{-1}$ g$^{-1}$ under simulated solar light irradiation, which is 15.5 times than that of bulk g-$C_3N_4$, as well as higher than most of the reported crystalline g-$C_3N_4$. Moreover, a highly apparent quantum efficiency of 9.01% at 420 nm for hydrogen evolution can be achieved, which is also superior to the reported crystalline g-$C_3N_4$. Such two-step calcination approach not only provides an economical way to effectively regulate the crystallinity of bulk g-$C_3N_4$, but also achieves the preparation of CCNNSs with high yield. Our research opens up a new window to self-modification and fabrication of highly active metal-free photocatalysts for solar light-driven hydrogen production.

## 1. Introduction

Semiconductor-based photocatalysis driven by solar light has been considered as an attractive and ideal solution to the global energy crisis and environmental pollution [1–5]. Among various available semiconductors, graphitic carbon nitride (g-$C_3N_4$) has emerged as a promising metal-free visible-light photocatalyst owing to the facts that it can work under visible light (2.7 eV) and the preparation approach is green and cost-effective [6–8]. However, the photocatalytic performance of bulk graphitic carbon nitride is far from satisfaction, principally due to its low visible-light absorption and quantum yield, low crystallinity, nominal specific surface area and rapid recombination of radiative charge carriers [9–12]. To challenge these limitations, various approaches have been proposed, including exfoliation of bulk carbon nitride into two-dimensional nanosheets [13,14], electronic structure modulation [15], nanostructure design [16–21], elemental doping [22,23], heterostructure construction [24–27] and reaction environment modulation [28,29].

To date, the widely used method to synthesize the graphitic carbon nitride is based on the traditional solid-state thermal condensation of nitrogen-rich precursors, which results in poor crystallinity and structural defects due to incomplete reacted intermediates including the amino or cyano groups during the condensation process [30,31]. The photocatalytic performance of g-$C_3N_4$ is sensitively affected by these residual functionalities, which often act as charge trap sites in photocatalytic chemical reactions [32–34]. Moreover, the carbon nitride nanosheets with abundant intralayer hydrogen bonds in the covalent carbon nitride framework as photocatalysts suffer from an additionally high localization of radiative charge carriers within each melon strand and thus leads to poor intralayer transport [35,36]. To this end, various strategies have been devised to prepare crystalline g-$C_3N_4$ nanosheets (CCNNSs) photocatalyst based on poly (triazine imides) (PTI) or poly (tri-s-triazine). Thanks to the improved crystallinity, the photocatalytic hydrogen evolution activity of CCNNSs can be enhanced with respect to bulk g-$C_3N_4$. For instance, Lin et al. [34] designed highly crystalline g-$C_3N_4$ by judiciously combining the melamine–cyanuric acid supramolecular aggregates and microwave assisted thermolysis. Under the optimum microwave reaction time, the resulting highly crystalline g-$C_3N_4$ displayed excellent photocatalytic hydrogen evolution activity, which is two times higher than that of a g-$C_3N_4$ sample obtained by thermal

---

polycondensation. Wang et al. [36] demonstrated a conventional and cost-effective synthesis of tri-*s*-triazine-based CCNNSs by liquid phase exfoliation through a sonication method. As expected, the as-prepared CCNNSs exhibited a high apparent quantum efficiency of 8.57% at 420 nm. Bhunia et al. [17] synthesized crystalline $g$-$C_3N_4$ via two-step rearrangement procedure by combining both supramolecular pre-organization and ionic melt polycondensation by employing melamine and 2,4,6-triaminopyrimidine as a chemically suitable dopant. The confined growth of $g$-$C_3N_4$ in an anodic aluminum oxide (AAO) membrane template has also resulted in improving the crystallinity [37]. However, the above-mentioned methods to construct crystalline $g$-$C_3N_4$ can suffer from some demerits, such as high synthetic cost and low yield [11]. Therefore, it is essential to develop simple and economic strategy for the rational synthesis of $g$-$C_3N_4$ photocatalyst with improved crystallinity.

In this work, we reported first-time two-step thermal treatment route for the preparation of highly crystalline $g$-$C_3N_4$ nanosheets (CCNNSs) photocatalyst. Note that such two-step calcination approach can be used to produce CCNNSs with high yield under the absence of any additives, toxic solvents or pre-intercalation steps. The detailed synthetic process is shown in Fig. 1. Bulk $g$-$C_3N_4$ (BCN) was prepared by the polycondensation of dicyandiamide. It is worth noting that the most obvious feature of this layered BCN from other layered compounds is the presence of abundant hydrogen bonds in the covalent bonding dominated intralayer framework (Fig. 1), which is due to the incomplete polymerization of the precursors containing amine groups during the polycondensation process. Next, BCN was used as the starting material to produce CCNNSs by heating BCN in targeted reaction temperature in an atmosphere of argon by judiciously wrapping the alumina boat crucible with aluminum foil (Fig. S1). During this thermal treatment, plenty of intralayer hydrogen bonds can be broken to form extended π-conjugated systems, which results in an improved crystallinity. Additionally, since the reagent is not able to escape from the completely wrapped aluminum foil, a high yield production of crystalline $g$-$C_3N_4$ (~85%) is achieved (Fig. S1), which is superior to that of the previous reported works for the photocatalytic hydrogen production (Table S1). The resultant CCNNSs offered the advantages of cost-effectiveness, easy scale up, and environmental friendliness, which exhibit significantly enhanced photocatalytic water reduction and rhodamine B (RhB) degradation activities under solar light irradiation.

## 2. Experimental section

### 2.1. Preparation of conventional bulk $g$-$C_3N_4$ photocatalyst

In general, conventional bulk $g$-$C_3N_4$ (BCN) sample was prepared by the polycondensation of dicyandiamide within a crucible at 520 °C for 4 h with a ramp rate of 2 °C/min in air. The resulting yellow products were named BCN and milled into powder with a mortar and pestle before further use.

### 2.2. Preparation of highly crystalline $g$-$C_3N_4$ nanosheets photocatalyst

The highly crystalline graphitic carbon nitride nanosheets (CCNNSs) were prepared by heating the bulk $g$-$C_3N_4$ by completely wrapping the alumina boat containing the sample with aluminum foil (as shown in Fig. S1) at 620 °C for 2 h with a ramping rate of 2 °C/min under continuous flow of argon in a tube furnace. The as-prepared crystalline carbon nitride nanosheets samples were named as CCNNSs.

Note: The complete wrapping of the sample as describe in above is the guarantee of the success of experiment otherwise it will be resulted into low yield and an amorphous carbon nitride.

### 2.3. Characterization of material

XRD analysis of the as-prepared bulk $g$-$C_3N_4$ and crystalline $g$-$C_3N_4$ nanosheets samples were carried out at room temperature with a Rigaku D/MAX 2550 VB/PC apparatus applying Cu Kα radiation ($\lambda = 1.5406$ Å) and a graphite monochromator at 40 kV and 30 mA. The scanning electron microscopy (SEM) images were obtained by a Nova Nano SEM 450 scanning electron microscope at an acceleration voltage of 5 kV. A TEM JEM2000EX device using an accelerating voltage of 200 kV obtained transmission electron microscopy (TEM) images. The optical absorption spectra were recorded on a UV–vis spectrophotometer (Varian Cary 500) in the diffuse reflectance mode. The FTIR spectra were analysed with KBr disks holding the powder sample by using an FT-IR spectrometer (Nicolet Magna 550). The solid-state $^{13}C$ CP-MAS nuclear magnetic resonance (NMR) spectra were recorded on a Bruker Advance III 500 spectrometer. The composition and chemical states of the samples were analysed using X-ray photoelectron spectroscopy (PerkinElmer PHI 500 °C ESCA system with Al Kα radiation at 250 W). All binding energies were referenced to the C 1s peak
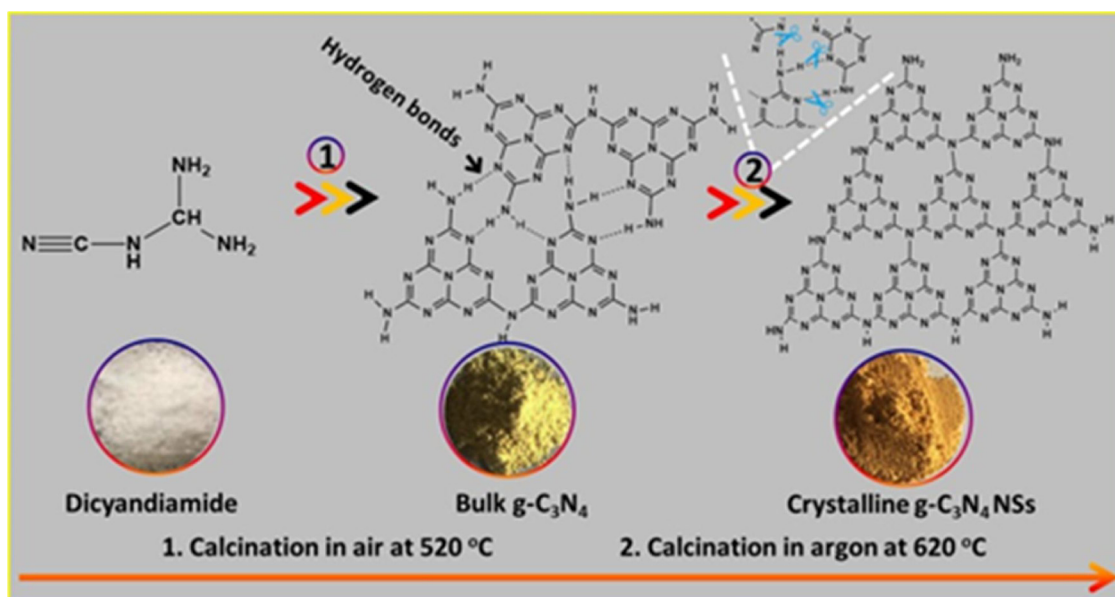


**Fig. 1.** The process of preparation of crystalline $g$-$C_3N_4$ NSs.

(284.6 eV) arising from adventitious carbon. The photoluminance spectra of the g-$C_3N_4$ samples were tested at room temperature excited by an incident light of 360 nm by using a spectrofluorophotometer (Shimadzu, RF–5301) with a Xe lamp as the excitation source. Steady and time-resolved fluorescence emission spectra were recorded at room temperature with a fluorescence spectrophotometer (Edinburgh Instruments, FLSP-920). The Brunauer–Emmett–Teller (BET) specific surface areas of the g-$C_3N_4$ samples were examined based on nitrogen adsorption isotherms measured at 77 K using a gas adsorption apparatus ASAP2020.

### 2.4. Photocatalytic hydrogen measurement

The photocatalytic hydrogen evolution experiments were conducted on an online photocatalytic hydrogen evolution system (Perfectlight, Beijing LabSolarIIIAG) at ambient temperature (5 °C) using a 300 W Xe lamp equipped with a AM 1.5 solar simulator. 50 mg of the g-$C_3N_4$ photocatalyst powder was dispersed in 100 mL aqueous solution containing 10 vol% triethanolamine (TEOA) as an electron donor. The deposition of 3 wt% Pt as a reducing co-catalyst was accomplished by dissolving $H_2PtCl_6$ in the above 100 mL reaction solution, which was in situ photo-reduced during the photocatalytic reaction. A 300 W Xe lamp equipped with an AM 1.5 air mass filter was used to irradiate the reaction solution. The photocatalytic hydrogen generation rate was measured by GC-7890 (TianMei) instrument with a thermal conductivity detector (TCD) and high-purity Ar as the carrier gas.

### 2.5. Photocatalytic degradation experiment

Rhodamine B was also employed as a model pollutant to measure the photocatalytic activity of as-synthesized samples. In a typical photocatalytic experiment, 50 mg photocatalyst was added in 50 mL of 20 mg $L^{-1}$ RhB aqueous solution. A 300 W Xe lamp with a 1.5 AM filter provided simulated solar irradiation. Prior to the light irradiation, the dispersion was kept in dark for 30 min under stirring to reach the adsorption–desorption equilibrium. During the photocatalytic tests, 3 mL of the sample was taken at a given time intervals, and centrifuged at 10,000 rpm for 5 min to remove the photocatalysts. Finally, the degradation results were monitored by the absorption intensity at 554 nm with a UV–vis spectrophotometer (Shimadzu UV-2450).

## 3. Results and discussion

The X-ray diffraction (XRD) patterns of as-prepared BCN and CCNNSs are shown in Fig. 2a. The two main characteristic diffraction peaks examined around at 2θ = 27.4° and 13.1° were indexed to (002) and (100) planes of hexagonal g-$C_3N_4$ (JCPDS card no. 87-1526), respectively, corresponding to the stacking of conjugated aromatic system and the in-plane tri-*s*-triazine stacking structural packing motifs in the conjugated aromatic units of g-$C_3N_4$ [38]. The wide diffraction peak of the BCN reveals that BCN produced by one-step conventional heating treatment has a low crystallinity. Compared with the BCN, the peak originated from the periodic stacking of layers in the crystalline graphitic carbon nitride nanosheets became sharper and shifted from 27.33° to 27.85°, demonstrating a decreased gallery distance between the basic sheets in the crystalline nanosheets. Distinctly, the amplified XRD peak intensity and the decreased interlayer distance upon heating the BCN at elevated temperature by technically wrapping the sample in alumina boat, has resulted in the improved polycondensation and formed highly CCNNSs. Interestingly, after heating BCN in the absence of Al foil wrapping at 620 °C, the carbon nitride structure buckled and transformed into the amorphous g-$C_3N_4$ with only short and broad peak at 27.2° (Fig. S2). Moreover, if dicyandiamide was directly calcinated with a wrapping at 620 °C in the argon atmosphere, we can obtain BCN rather than CCNNSs. It further indicates that when we only adjust the calcination temperature or atmosphere, it is difficult to achieve the

highly CCNNSs by one-step heating process.

The structure of CCNNSs can be further confirmed by Fourier transform infrared spectroscopy (FTIR). As demonstrated in Fig. 2b, the typical IR spectrum of the CCNNSs is similar to that of the BCN. The sharp peak about 807 $cm^{-1}$ is assigned to typical breathing mode of the triazine units. These peaks in the region from 1200 to 1600 $cm^{-1}$ represent characteristic stretching modes of CN heterocycles [39]. The broad peaks between 3000 and 3600 $cm^{-1}$ are produced by N−H stretching. All the peaks of CCNNSs are sharper than those of BCN, which is triggered by the more ordered packing of tri-*s*-triazine motifs at high temperature in the CCNNSs [16,40]. The structure of CCNNSs was further investigated by Solid-state $^{13}$C CP/MAS NMR spectroscopy (Fig. S3). Two distinct peaks were observed at 162.8 and 156.2 ppm. The first resonance was ascribed to the C (e) atoms ($N_2$–CN or terminal $CN_2$ (NHx)), and the second resonance was attributed to the C (i) atoms ($CN_3$), which confirmed the presence of tri-*s*-triazine units in the framework of CCNNSs [34,36]. Moreover, elemental analysis was done to further verify the percentage of C and N atoms in the BCN and CCNNSs (Table S2). The C/N ratios of the BNC and CCNNSs were determined to be 0.656 and 0.699, respectively, demonstrating a better condensation of the residual amino group and tri-*s*-triazine structure in the CCNNSs than the BCN sample.

The morphologies of CCNNSs and BCN samples were investigated by scanning electron microscope (SEM) and transmission electron microscope (TEM) observations. BCN appears to be dense and thick layers to form a massive structure (Fig. S4) while the morphology and microstructure of the obtained CCNNSs are changed dramatically at high temperature. CCNNSs possess thin structure with loose and porous morphology (Fig. 2c). The g-$C_3N_4$ nanosheets produced by two-step thermal treatment were further confirmed by TEM images (Fig. 2d). The inset in Fig. 2d allows us to observe the crystal lattice with a spacing of 3.30 Å, corresponding to the (002) interplanar distance in a standard layered carbon nitride crystal. The high temperature of 620 °C with the assistance of aluminum foil as a cover has resulted in minimum loss of the products due to sublimation and caused the exfoliation of bulk carbon nitride materials to form the fully condensed two dimensional highly CCNNSs. This simple synthesis strategy results in 85% of yield and highlights the substantial role of this combinative system in producing the distinctive texture of highly crystalline graphitic carbon nitride nanosheets. Additionally, compared to the traditional salt intercalation approaches, the synthesis involved here is cost-effective, environmentally benign method and is suitable for large-scale synthesis. The compositions and chemical states of the BCN and CCNNSs were investigated by X-ray photoelectron spectroscopy (XPS) analysis. The survey XPS spectra (Fig. S5a) reveal both of BCN and CCNNSs samples are predominantly composed of C and N elements. In addition, no obvious binding energy shift of C 1s and N 1s core electrons were observed (Fig. S5b,c), suggesting that the chemical states of both carbon and nitrogen in the crystalline nanosheets are the same as in the BCN [36]. Moreover, to rule out the existence of Al atom in the CCNNSs matrix, we performed the XPS analysis of Al (Fig. S6) that showed no Al species in the samples, which supported the fact that aluminum foil only used as a wrapping agent rather than Al doping of CCNNSs.

The effective transfer of the radiative charge carriers depends sensitively on the crystallization degree in the semiconductor photocatalysts, which are directly associated to the structural defects of the material. The separation and recombination behavior of the radiated charge carriers were first examined by photoluminescence (PL) spectra acquired at an excitation wavelength of 400 nm at room temperature. As demonstrated in Fig. 3a, BCN displays a strong and broad emission peak centered at about 455 nm corresponding to the inherent PL emission of BCN attributed by the rapid recombination of photogenerated charge carriers. On the contrary, the CCNNSs demonstrate the relatively very low emission intensity under the same conditions, indicating discernible suppressed recombination of the radiative charge carriers in the CCNNSs.
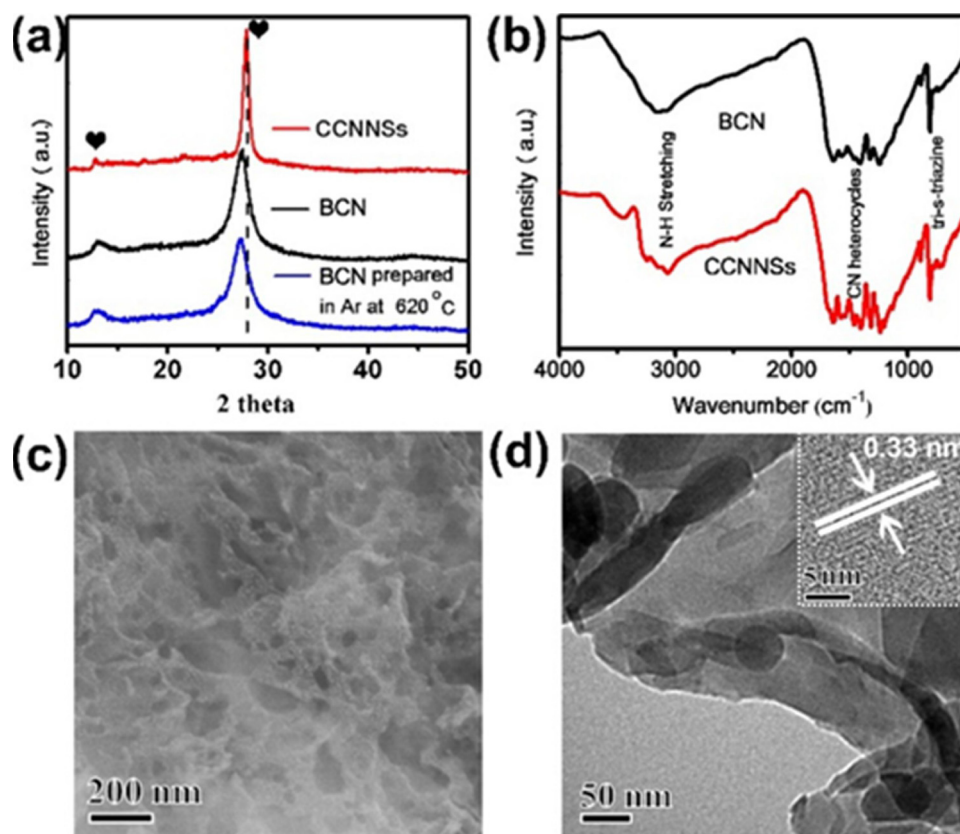
**Fig. 2.** (a) XRD patterns of as-prepared samples. (b) FTIR spectra of CCNNSs and BCN. SEM (c) and TEM (d) images of CCNNSs. The inset in (d) shows the HRTEM image of CCNNSs.
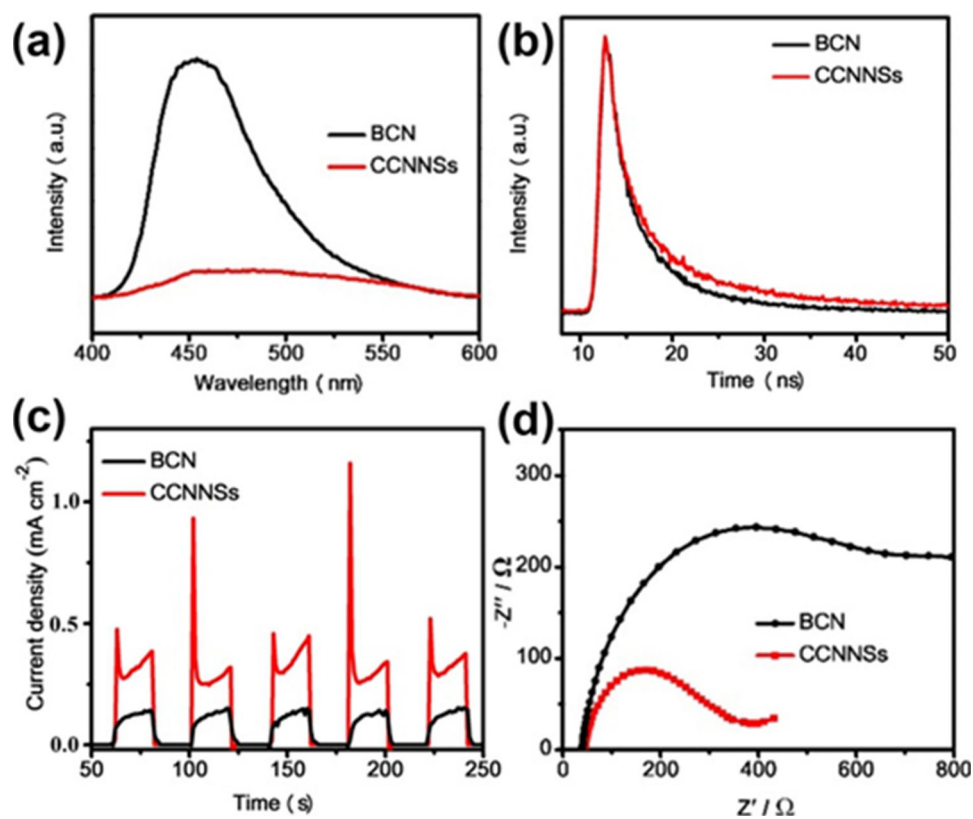


**Fig. 3.** (a) Photoluminescence spectra of as-prepared samples: BCN and CCNNSs. (b) Time-resolved Fluorescence decay spectra of BCN and CCNNSs. (c) Transit photo-current response of BCN and CCNNSs. (d) EIS Nyquist plots of BCN and CCNNSs.

The time-resolved fluorescence decay spectra of the BCN and highly CCNNSs were also tested. As shown in Fig. 3b, it is obvious that the fluorescent intensity of the CCNNSs showed slow decay kinetics as compared to its BCN counterpart. The three radiative lifetime constants $\tau1$, $\tau2$ and $\tau3$ of CCNNSs are 1.4197, 5.1430, and 19.0946 ns, respectively, which are all extended than the subsequent values for BCN (Table S3). These domino effects signify that the radiative lifespan of the photogenerated charge carriers has been improved in CCNNSs that play an imperative part in increasing the possibility of their partaking in photocatalytic chemical reactions rather than recombination. Additionally, it is accepted as true that the prolonged lifespans of radiative charge carriers are related to the better electrons mobility as demonstrated in CCNNSs [41].

In addition to the prolonged lifetime, the transfer efficiency of charges is another important influence factor on the photocatalytic performance of catalyst. We also measured the photoelectric response tests in BCN and CCNNSs samples to further evaluate the efficient separation of radiative charge carriers which were recorded for several on-off cycles of intermittent irradiation (Fig. 3c). Regardless of the comparatively small value, the photocurrent produced in the CCNNSs sample was still relatively large as compared to that in BCN, distinctly corroborating the efficient separation of radiative charge carriers and an improved photogenerated charge mobility in CCNNSs. In theory, the higher crystallinity of g-$C_3N_4$ means the smaller impedance of catalyst. As seen from Fig. 3d, the decreased semi-circular arc radius of Nyquist plot for CCNNSs suggests a smaller charge transfer resistance of CCNNSs than that of BCN.

The photocatalytic activity of the BCN and CCNNSs were first evaluated by investigating the photocatalytic hydrogen evolution, which was carried out under simulated solar light in a water/triethanolamine solution, and 3 wt% Pt was used as a cocatalyst. As

demonstrated in Fig. 4a, the average $H_2$ evolution rate of the CCNNSs under simulated solar light is 9577.6 $\mu mol\,h^{-1}\,g^{-1}$, which is substantially higher than that of BCN (618.2 $\mu mol\,h^{-1}\,g^{-1}$) and most of the reported crystalline g-$C_3N_4$ (as shown in Table S1: 1060–8160 $\mu mol\,h^{-1}\,g^{-1}$). We believe that the photocatalytic $H_2$ evolution rate of CCNNSs are a much higher than some previously reported crystalline 2D g-$C_3N_4$ nanosheets and other typical nanostructured g-$C_3N_4$ photocatalysts [34,40,42,43]. Moreover, the $H_2$ production rate of CCNNSs after 5 cycling is sustained (Fig. 4a), which results from the excellent physiochemical stability of inherent structure for CCNNSs as shown from Fig. S7. Fig. 4b demonstrates the wavelength dependence of the apparent quantum efficiency (AQE) values of CCNNSs for $H_2$ evolution, which indicates the correspondence of the variation tendency of the AQE curve with their diffuse reflectance spectra (DRS) curves. The AQE value at 420 nm reaches up to 9.01%, which is superior to most reported crystalline $C_3N_4$ [31,36]. These results fully exhibit the hydrogen evolution rate heavily relies on the wavelength of the incident light. Additionally, CCNNSs also demonstrate superior photodegradation ability for RhB pollutant under simulated light irradiation. RhB is very stable under visible light irradiation. Obviously, almost all RhB can be degraded after 20 min simulated solar light irradiation over CCNNSs. For comparison, only about 5% of RhB are removed under the same conditions by using BCN and the RhB degradation efficiency of CCNNSs is nearly 20 times higher than that of BCN (Fig. 3c). The recycling experiment were also performed for the photodegradation of RhB over CCNNSs (Fig. S8) which did not show a significant decrease after four recycles, indicative of the excellent stability of the CCNNSs. Furthermore, the apparent degradation rate constants (K) for the photodegradation of RhB were also calculated (Fig. 3d). The K of CCNNSs ($4.04 \times 10^{-2}\,min^{-1}$) is 100 times higher than that of BCN ($4.02 \times 10^{-4}\,min^{-1}$). That means the highly
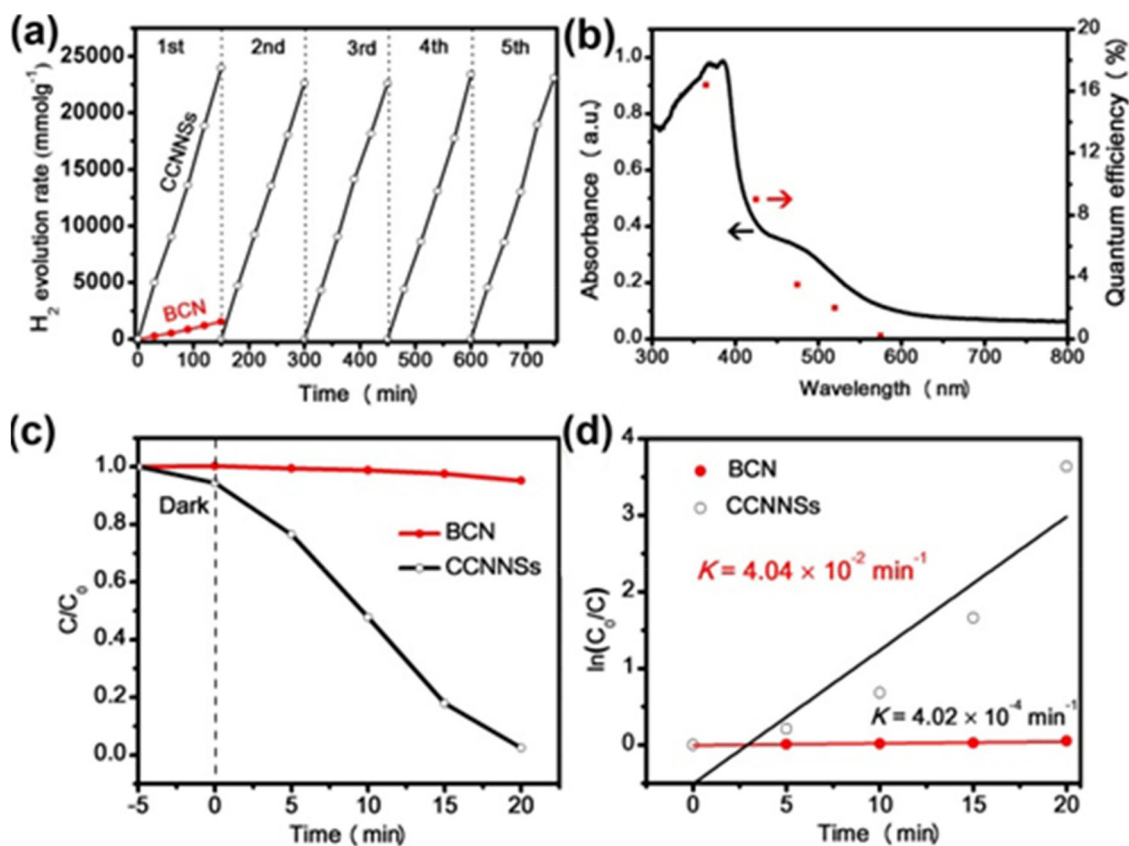


**Fig. 4.** (a) Photocatalytic hydrogen evolution reactions of as-prepared samples: CCNNSs and BCN under simulated solar light irradiation (AM 1.5G). (b) Wavelength-dependent AQE of $H_2$ evolution over CCNNSs. (c) Photocatalytic oxidation of RhB for BCN and CCNNSs and (d) the corresponding kinetic rate constants (K) calculation under the simulated solar light irradiation.

crystalline g-C$_3$N$_4$ has a large potential to be application in the photo-degradation of organic pollutants.

It is necessary to investigate the potential contribution of the surface area increment of the g-C$_3$N$_4$ product to their enhanced photocatalytic hydrogen evolution performance. The CCNNSs have specific surface area of 34 m$^2$ g$^{-1}$, whereas the BCN has a surface area of only 6.5 m$^2$ g$^{-1}$ (Fig. S9). Although the larger surface area often provides more exposed edges and catalytic sites, a fact, which are beneficial for improved electron transportability and rapid cross-plane diffusion of photogenerated charge carriers, however, the surface area-normalized activity with respect to the specific surface area is usually lowered. For example, the retention percentage of the normalized activity of the proton-activated carbon nitride as compared to the pristine carbon nitride was less than 100% [35,44]. In our case, as for CCNNSs, its specific surface area improved by a factor of around 5 from the pristine 6.5 to 34 is definitely beneficial to the photocatalysis, but cannot be responsible for such high enhancement of photocatalytic hydrogen evolution activity by a factor of around 16 from the pristine 618.2 to 9577.6 μmol g$^{-1}$ h$^{-1}$. Compared with BCN, the retention percentage of the surface area-normalized hydrogen evolution of CCNNSs increased up to 296%. As a result, such high photocatalytic hydrogen production activity is dominantly caused by the high crystallinity and low surface defect density rather than the enhanced specific surface area.

The efficiency of a photocatalyst is determined by the three main steps in the photocatalytic process: light absorption, charge separation and surface redox reaction. In our case, the CCNNSs showed the broader and stronger visible light absorption than BCN most likely due to the enhanced crystallinity and the extended π-conjugated systems

(Fig. 5a), which is similar to that of the conjugated graphene with high light-harvesting efficiency. Accordingly, the derived bandgaps of the light absorbed for CCNNSs and BCN were 2.23 eV and 2.81 eV, respectively (inset of Fig. 5a), which is in good agreement with the color of the samples. The valence band (VB) positions of both BCN and CCNNSs were determined by the XPS valence spectra (Fig. S10). As demonstrated in, CCNNSs decreased to 0.15 eV as compared to BCN (2.10 eV vs. 2.25 eV). Based on the bandgaps in Fig. 5a, the conduction bands (CB) of CCNNSs were estimated to be downshifted by 0.43 eV, as shown in Fig. 5b. The obvious shift of CB and VB of CCNNSs decrease the reduction ability of photogenerated electrons and the oxidation ability of holes. However, from the result of photocatalytic hydrogen evolution reactions, the hydrogen evolution rate of CCNNSs is much superior to that of BCN, which further suggests that the improved crystallinity has overcome the decrease of redox potential to play a dominant role in photocatalytic hydrogen evolution reactions.

In our case, triethanolamine (TEOA) and Pt nanoparticles were used as the holes sacrificial agent and reaction center respectively, for the H$_2$ evolution. Owing to the surrounding weakly alkaline environment, free H$^+$ ions are hardly existing. The reaction is supposed to proceed through the Volmer–Heyrovsky or Volmer–Tafel pathways [45,46]. That is the H$_2$ production is in the form of direct reduction of adsorbed H$_2$O molecules, instead of dissociated H$^+$ ions [47]. Seen from Fig. 5c, the BCN displays a low electrons transfer efficiency due to the low crystallinity. A mass of intralayer hydrogen bonds in BCN suffer from an additionally higher localization of radiative charge carriers within each melon strand and thus leads to poor intralayer transport, which might introduce the recombination centers for the photo-generated electrons
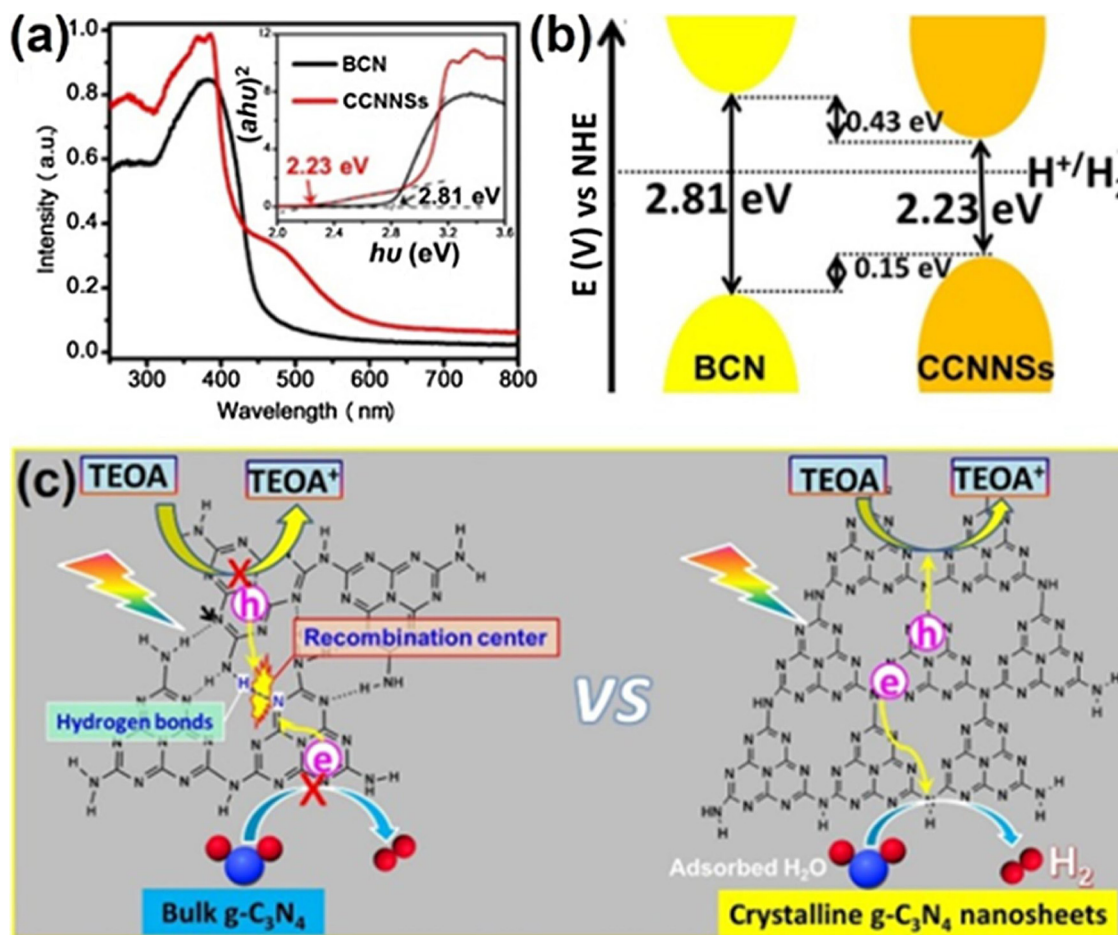


**Fig. 5.** (a) UV–vis DRS spectra of BCN and CCNNSs (inset is the Plots of $(ah\nu)^2$ versus the energy of exciting light). (b) Electronic band structure of BCN and CCNNSs. (c) Schematic illustration of the suggested mechanism of H$_2$ evolution over BCN and CCNNSs.

and holes. Separately, the CCNNSs have the high crystallinity with long-range ordered lattice structure, which is very beneficial for the transfer of electrons from g-$C_3N_4$ to Pt. As the result, the photogenerated electrons were transferred to Pt nanoparticles, which are served as the reaction centers for $H_2O$ reduction and $H_2$ evolution.

## 4. Conclusions

In conclusion, we have presented a novel and economic strategy for the synthesis of highly crystalline carbon nitride nanosheets, which act as highly efficient photocatalyst for $H_2$ evolution from water by using solar energy. A detailed characterization described that this simple synthetic strategy not only improved the crystallinity of g-$C_3N_4$ sample with enhanced visible absorption but also improved the radiative charge carrier mobility. This work highlights that an easy and green route can be utilized to synthesize a high-efficiency crystalline g-$C_3N_4$ nanosheets photocatalyst without employing any toxic solvent or salt intercalation steps, which opens up a new window to self-modification and fabrication of highly active metal-free photocatalysts for solar light-driven hydrogen production and can be extended to other solar energy applications, such as $CO_2$ photofixation, organic photosynthesis, as well as organic pollutants degradation.

## Competing financial interest

The authors declare no competing financial interest.

## Acknowledgments

## Appendix A. Supplementary data

Supplementary material related to this article can be found, in the online version, at doi:https://doi.org/10.1016/j.apcatb.2018.03.072.

## References

[1] B. Qiu, M. Xing, J. Zhang, Mesoporous $TiO_2$ nanocrystals grown in situ on graphene aerogels for high photocatalysis and lithium-ion batteries, J. Am. Chem. Soc. 136 (2014) 5852–5855.

[2] M. Waqas, S. Iqbal, A. Bahadur, A. Saeed, M. Raheel, M. Javed, Designing of a spatially separated hetero-junction pseudobrookite ($Fe_2 TiO_5$ -$TiO_2$) yolk-shell hollow spheres as efficient photocatalyst for water oxidation reaction, Appl. Catal. B: Environ. 219 (2017).

[3] M. Xing, B. Qiu, M. Du, Q. Zhu, L. Wang, J. Zhang, Spatially separated CdS shells exposed with reduction surfaces for enhancing photocatalytic hydrogen evolution, Adv. Funct. Mater. 27 (35) (2017).

[4] B. Qiu, Q. Zhu, M. Du, L. Fan, M. Xing, J. Zhang, Efficient solar light harvesting CdS/$Co_9S_8$ hollow cubes for z-scheme photocatalytic water splitting, Angew. Chem. 129 (2017) 2728–2732.

[5] B. Qiu, Q. Zhu, M. Xing, J. Zhang, A robust and efficient catalyst of Cd x Zn 1-x Se motivated by CoP for photocatalytic hydrogen evolution under sunlight irradiation, Chem. Commun. 53 (2017) 897–900.

[6] X. Wang, K. Maeda, A. Thomas, K. Takanabe, G. Xin, J.M. Carlsson, K. Domen, M. Antonietti, A metal-free polymeric photocatalyst for hydrogen production from water under visible light, Nat. Mater. 8 (2009) 76–80.

[7] Y. Wang, X. Wang, M. Antonietti, Polymeric graphitic carbon nitride as a heterogeneous organocatalyst: from photochemistry to multipurpose catalysis to sustainable chemistry, Angew. Chem. Int. Ed. 51 (2012) 68–89.

[8] Y. Zheng, J. Liu, J. Liang, M. Jaroniec, S.Z. Qiao, Graphitic carbon nitride materials: controllable synthesis and applications in fuel cells and photocatalysis, Energy Environ. Sci. 5 (2012) 6717–6731.

[9] F. Wu, Y. Liu, G. Yu, D. Shen, Y. Wang, E. Kan, Visible-light-absorption in graphitic $C3N_4$ bilayer: enhanced by interlayer coupling, J. Phys. Chem Lett. 3 (2012) 3330–3334.

[10] C. Liu, L. Jing, L. He, Y. Luan, C. Li, Phosphate-modified graphitic $C_3N_4$ as efficient photocatalyst for degrading colorless pollutants by promoting $O_2$ adsorption, Chem. Commun. 50 (2014) 1999–2001.

[11] X.-H. Li, J. Zhang, X. Chen, A. Fischer, A. Thomas, M. Antonietti, X. Wang, Condensed graphitic carbon nitride nanorods by nanoconfinement: promotion of crystallinity on photocatalytic conversion, Chem. Mater. 23 (2011) 4344–4348.

[12] H. Li, L. Wang, Y. Liu, J. Lei, J. Zhang, Mesoporous graphitic carbon nitride materials: synthesis and modifications, Res. Chem. Intermed. 42 (2016) 3979–3998.

[13] W. Xing, G. Chen, C. Li, J. Sun, Z. Han, Y. Zhou, Y. Hu, Q. Meng, Construction of large-scale ultrathin graphitic carbon nitride nanosheets by a hydrogen-bond-assisted strategy for improved photocatalytic hydrogen production and ciprofloxacin degradation activity, ChemCatChem 8 (2016) 2838–2845.

[14] W. Iqbal, B. Qiu, J. Lei, L. Wang, J. Zhang, M. Anpo, One-step large-scale highly active g-$C_3N_4$ nanosheets for efficient sunlight-driven photocatalytic hydrogen production, Dalton Trans. 46 (2017) 10678–10684.

[15] Y. Zheng, Y. Jiao, M. Jaroniec, S.Z. Qiao, Advancing the electrochemistry of the hydrogen-evolution reaction through combining experiment and theory, Angew. Chem. Int. Ed. 54 (2015) 52–65.

[16] S. Yang, Y. Gong, J. Zhang, L. Zhan, L. Ma, Z. Fang, R. Vajtai, X. Wang, P.M. Ajayan, Exfoliated graphitic carbon nitride nanosheets as efficient catalysts for hydrogen evolution under visible light, Adv. Mater. 25 (2013) 2452–2456.

[17] M.K. Bhunia, K. Yamauchi, K. Takanabe, Harvesting solar light with crystalline carbon nitrides for efficient photocatalytic hydrogen evolution, Angew. Chem. 126 (2014) 11181–11185.

[18] Y.S. Jun, J. Park, S.U. Lee, A. Thomas, W.H. Hong, G.D. Stucky, Three-dimensional macroscopic assemblies of low-dimensional carbon nitrides for enhanced hydrogen evolution, Angew. Chem. 125 (2013) 11289–11293.

[19] D.J. Martin, K. Qiu, S.A. Shevlin, A.D. Handoko, X. Chen, Z. Guo, J. Tang, Highly efficient photocatalytic $H_2$ evolution from water using visible light and structure-controlled graphitic carbon nitride, Angew. Chem. Int. Ed. 53 (2014) 9240–9245.

[20] Y. Zhang, A. Thomas, M. Antonietti, X. Wang, Activation of carbon nitride solids by protonation: morphology changes, enhanced ionic conductivity, and photo-conduction experiments, J. Am. Chem. Soc. 131 (2009) 50.

[21] W. Iqbal, C. Dong, M. Xing, X. Tan, J. Zhang, Eco-friendly one-pot synthesis of well-adorned mesoporous g-$C_3N_4$ with efficiently enhanced visible light photocatalytic activity, Catal. Sci. Technol. 7 (2017) 1726–1734.

[22] Y. Zhang, T. Mori, J. Ye, M. Antonietti, Phosphorus-doped carbon nitride solid: enhanced electrical conductivity and photocurrent generation, J. Am. Chem. Soc. 132 (2010) 6294–6295.

[23] X. Chen, J. Zhang, X. Fu, M. Antonietti, X. Wang, Fe-g-$C_3N_4$-catalyzed oxidation of benzene to phenol using hydrogen peroxide and visible light, J. Am. Chem. Soc. 131 (2009) 11658–11659.

[24] L. Zhou, L. Wang, J. Zhang, J. Lei, Y. Liu, Well-dispersed Fe2O3 nanoparticles on g-$C_3N_4$ for efficient and stable photo-fenton photocatalysis under visible-light irradiation, Eur. J. Inorg. Chem. 2016 (2016) 5387–5392.

[25] R. Asahi, T. Morikawa, T. Irie, T. Ohwaki, Nitrogen-doped titanium dioxide as visible-light-sensitive photocatalyst: designs, developments, and prospects, Chem. Rev. 114 (2014) 9824–9852.

[26] G. Li, X. Nie, J. Chen, Q. Jiang, T. An, P.K. Wong, H. Zhang, H. Zhao, H. Yamashita, Enhanced visible-light-driven photocatalytic inactivation of Escherichia coli using g-$C_3N_4$/$TiO_2$ hybrid photocatalyst synthesized using a hydrothermal-calcination approach, Water Res. 86 (2015) 17–24.

[27] G. Li, N. Xin, Y. Gao, T. An, Can environmental pharmaceuticals be photo-catalytically degraded and completely mineralized in water using g-$C_3N_4$/$TiO_2$ under visible light irradiation? Implications of persistent toxic intermediates, Appl. Catal. B: Environ. 180 (2016) 726–732.

[28] P. Wu, J. Wang, J. Zhao, L. Guo, F.E. Osterloh, High alkalinity boosts visible light driven $H_2$ evolution activity of g-$C_3N_4$ in aqueous methanol, Chem. Commun. 50 (2014) 15521–15524.

[29] G. Liu, T. Wang, H. Zhang, X. Meng, D. Hao, K. Chang, P. Li, T. Kako, J. Ye, Nature-inspired environmental "Phosphorylation" boosts photocatalytic $H_2$ production over carbon nitride nanosheets under visible-light irradiation, Angew. Chem. 127 (2015) 13765–13769.

[30] Z. Lin, X. Wang, Nanostructure engineering and doping of conjugated carbon nitride semiconductors for hydrogen photosynthesis, Angew. Chem. Int. Ed. 52 (2013) 1735–1738.

[31] M.K. Bhunia, K. Yamauchi, K. Takanabe, Harvesting solar light with crystalline carbon nitrides for efficient photocatalytic hydrogen evolution, Angew. Chem. Int. Ed. 53 (2014) 11001–11005.

[32] U. Diebold, Photocatalysts: closing the gap, Nat. Chem. 3 (2011) 271–272.

[33] L. Lin, H. Ou, Y. Zhang, X. Wang, Tri-s-triazine-based crystalline graphitic carbon nitrides for highly efficient hydrogen evolution photocatalysis, ACS Catal. 6 (2016) 3921–3931.

[34] Y. Guo, J. Li, Y. Yuan, L. Li, M. Zhang, C. Zhou, Z. Lin, A rapid microwave-assisted thermolysis route to highly crystalline carbon nitrides for efficient hydrogen generation, Angew. Chem. Int. Ed. 55 (2016) 14693–14697.

[35] Y. Kang, Y. Yang, L.C. Yin, X. Kang, L. Wang, G. Liu, H.M. Cheng, Selective breaking of hydrogen bonds of layered carbon nitride for visible light photocatalysis, Adv. Mater. 28 (2016) 6471–6477.

[36] H. Ou, L. Lin, Y. Zheng, P. Yang, Y. Fang, X. Wang, Tri-s-triazine-based crystalline carbon nitride nanosheets for an improved hydrogen evolution, Adv. Mater. 29 (2017).

[37] X.H. Li, J. Zhang, X. Chen, A. Fischer, A. Thomas, M. Antonietti, X. Wang,

Condensed graphitic carbon nitride nanorods by nanoconfinement: promotion of crystallinity on photocatalytic conversion, Chem. Mater. 23 (2011) 4344–4348.

[38] Y. Wang, J. Hong, W. Zhang, R. Xu, Carbon nitride nanosheets for photocatalytic hydrogen evolution: remarkably enhanced activity by dye sensitization, Catal. Sci. Technol. 3 (2013) 1703–1711.

[39] Q. Liang, Z. Li, X. Yu, Z.H. Huang, F. Kang, Q.H. Yang, Macroscopic 3D porous graphitic carbon nitride monolith for enhanced photocatalytic hydrogen evolution, Adv. Mater. 27 (2015) 4634–4639.

[40] Q. Liang, Z. Li, Z.H. Huang, F. Kang, Q.H. Yang, Holey graphitic carbon nitride nanosheets with carbon vacancies for highly improved photocatalytic hydrogen production, Adv. Funct. Mater. 25 (2015) 6885–6892.

[41] P. Niu, L. Zhang, G. Liu, H.M. Cheng, Graphene-like carbon nitride nanosheets for improved photocatalytic activities, Adv. Funct. Mater. 22 (2012) 4763–4770.

[42] K. Schwinghammer, M.B. Mesch, V. Duppel, C. Ziegler, Jr. Senker, B.V. Lotsch, Crystalline carbon nitride nanosheets for improved visible-light hydrogen evolution, J. Am. Chem. Soc. 136 (2014) 1730–1733.

[43] Y. Li, R. Jin, Y. Xing, J. Li, S. Song, X. Liu, M. Li, R. Jin, Macroscopic foam-like holey ultrathin g-C3N4 nanosheets for drastic improvement of visible-light photocatalytic activity, Adv. Energy Mater. 6 (2016).

[44] Y. Zhang, A. Thomas, M. Antonietti, X. Wang, Activation of carbon nitride solids by protonation: morphology changes, enhanced ionic conductivity, and photo-conduction experiments, J. Am. Chem. Soc. 131 (2008) 50–51.

[45] S.A. Vilekar, I. Fishtik, R. Datta, Kinetics of the hydrogen electrode reaction, J. Electrochem. Soc. 157 (2010) B1040–B1050.

[46] E. Skúlason, V. Tripkovic, M.E. Björketun, S. Gudmundsdottir, G. Karlberg, J. Rossmeisl, T. Bligaard, H. Jónsson, J.K. Nørskov, Modeling the electrochemical hydrogen oxidation and evolution reactions on the basis of density functional theory calculations, J. Phys. Chem. C 114 (2010) 18182–18197.

[47] M. Liu, Y. Chen, J. Su, J. Shi, X. Wang, L. Guo, Photocatalytic hydrogen production using twinned nanocrystals and an unanchored NiSx co-catalyst, Nat. Energy 1 (2016) 16151.